Journal of Materials Chemistry C

ROYAL SOCIETY OF CHEMISTRY

PAPER

View Article Online
View Journal | View Issue

Cite this: J. Mater. Chem. C, 2025, 13, 10640

A highly sensitive fluorescent nanofiber sensor functionalized with small organic molecules for specific analyte detection†

Leqin Cheng,[a] Yunqi Tao,[a] Jie Chen,[b] Xiaohan Zhu,[b] Zhonglin Wei,[c] Ding Zhou,[d] Yuewei Zhang *[a] and Xue Yu*[a]

Received 19th December 2024,
Accepted 18th April 2025

DOI: 10.1039/d4tc05358c

rsc.li/materials-c

The rapid, sensitive, and efficient detection of nitroaromatic explosives is crucial for human health and public safety, particularly in detecting trace explosive vapors. In this study, a donor–acceptor (D–A) type fluorescent probe, 6-(6-(9*H*-carbazol-9-yl)pyridin-3-yl)-2-phenyl-1*H*-benzo[*de*]isoquinoline-1,3(2*H*)-dione (**PPBD**), was synthesized by coupling carbazole and 1,8-naphthalimide *via* the Suzuki reaction. The probe exhibits characteristic intramolecular charge transfer (ICT) emission, which makes it highly efficient for detecting nitroaromatic explosives such as pentaerythritol tetranitrate (PETN), trinitrotoluene (TNT), 2-nitro-*m*-xylene cyclotetramethylene tetranitramine (HMX), and cyclotrimethylene trinitramine (RDX). Additionally, an electrospun fiber film of **PPBD**/PEO was fabricated, demonstrating high sensitivity in sensing nitroaromatic vapors *via* fluorescence testing. The quenching efficiencies for HMX, TNT, RDX, PETN, and 2-nitro-*m*-xylene are 92%, 89%, 76%, 64%, and 40%, respectively, with the highest selectivity for HMX vapor. This enhanced selectivity is attributed to the increased contact area between nanofibers and analytes in the film, facilitating effective fluorescence quenching. Proton transfer from analytes to **PPBD** blocks ICT emission, leading to the quenching of fluorescence.

1. Introduction

Terrorist bombings not only pose a serious threat to global security and social stability but also directly endanger human health and the ecological environment due to the leakage of explosives.[1–3] Therefore, the detection of explosives has become a critical concern in international security today. Currently, the technologies used for detecting explosives mainly include fluorescence detection technology,[4,5] ion mobility spectrometry,[6,7] surface-enhanced Raman spectroscopy technique,[8,9] portable Raman spectroscopy technology,[10,11] electrical atmosphere-sensing technology[12,13] and chemical colorimetric technology.[14,15] Among them, fluorescence detection technology has been widely applied in the field of explosive detection due to its high sensitivity, fast response speed, low cost, and good selectivity.[16,17]

Fluorescence-based detection of explosives typically involves the selective interaction between the explosive and a recognition group, which causes a change in the spectral signal of the fluorescent probe.[18] These changes include alteration in fluorescence spectral intensity (including quenching or enhancement), the shift in fluorescence spectral peaks, or the variation in fluorescence lifetime are utilized to achieve the detection of explosives.[19] Organic small molecule fluorescent probes, which are a significant class of fluorescent materials, exhibit various fluorescence quenching mechanisms, including photoinduced electron transfer (PET), fluorescence resonance energy transfer (FRET), and intramolecular charge transfer (ICT), these mechanisms enable the detection of explosives through fluorescence quenching.[20–25] In recent years, organic small molecule fluorescent probes have become a research hotspot in the fluorescent detection of explosive.[26,27]

However, these fluorescent probes mostly exist in solution form, limiting their practical application in real-world environments.[28] Utilizing electrospinning technology to fabricate nanofibers or porous nanomaterials can effectively address the shortcomings of solution-based fluorescent probes.[29–32] Electrospun fibrous membranes offer larger porosity and higher specific surface areas, which enhance interactions between fluorescent molecules and analytes, facilitating more effective fluorescence quenching.[23,33] The combination of electrospinning technology with organic small molecule fluorescent probes has led to the development of stable, portable,

[a] School of Chemistry and Pharmaceutical Engineering, Jilin Institute of Chemical Technology, Jilin 132022, China. E-mail: zhangyueweichem@163.com, dongjibinghuayuxue@163.com
[b] Forensic Center of Changchun Public Security Bureau, Changchun 130000, China
[c] College of Chemistry, Jilin University, Changchun 130012, P. R. China
[d] Jilin Provincial Key Laboratory of Tooth Development and Bone Remodeling, School and Hospital of Stomatology, Jilin University, Changchun 130021, P. R. China

† Electronic supplementary information (ESI) available. See DOI: https://doi.org/10.1039/d4tc05358c

and reusable fluorescent nanofiber membrane sensors. These sensors have been wide applications in bioimaging, food testing, and environmental analysis.[34,35]

This study design and synthesis of a novel carbazole-based fluorescent sensing compound, 6-(6-(9*H*-carbazol-9-yl)pyridin-3-yl)-2-phenyl-1*H*-benzo[*de*]isoquinoline-1,3-(2*H*)-dione (**PPBD**). **PPBD** is a D–A type molecule, composed of a 1,8-naphthalimide unit as the acceptor and a carbazole unit as the donor, with its emission attributed to ICT from the carbazole unit to the 1,8-naphthalimide unit. To incorporated **PPBD** into polyethylene oxide (PEO), a widely used and cost-effective polymer. This successful preparing a high-performance, low-cost explosive fluorescent sensor based on **PPBD**/PEO polymer fibers. When 0.5 wt% of **PPBD** is doped into PEO, the **PPBD**/PEO polymer luminescent fibers exhibit a fluorescence quenching efficiency as high as 92% when exposed to HMX vapor for 2 hours.

2. Experimental section

2.1. Experimental drugs and reagents

9*H*-Carbazol, aniline, 4-bromine-1,8-naphthalene diformic anhydride, 2-fluoro-5-bromopyridine, double-linked frequency which alcohol diboron, potassium acetate, cesium carbonate (Cs_2CO_3), 1,1′-bis-diphenylphosphine, ferrocene palladium dichloride ($Pd(dppf)Cl_2$), 1,1′-bis(diphenylphosphine) ferrocene (dppf), palladium(II) acetate ($Pd(OAc)_2$), cuprous chloride, polyethylene oxide (PEO), dimethyl sulfoxide (DMSO), 2-methoxyethanol, toluene, *N*,*N*-dimethylformamide (DMF), hexyl hydride, petroleum ether, ethyl acetate, trichloromethane ($CHCl_3$), acetone, methanol (MeOH), and alcohol (EtOH) were purchased from China Energy Chemical and used according to the instructions received, and the solvents were analytically pure.

2.2. Instruments and equipment

The Shimadzu UV-2550 double-beam spectrophotometer was used to measure the ultraviolet-visible absorption spectra, Fluorescence spectra were obtained using a Fluoromax Plus steady-state/lifetime fluorescence spectrometer, ^{1}H NMR and ^{13}C NMR spectra were acquired using a Bruker 400 MHz NMR spectrometer, fluorescence micrographs were obtained using a Nikon-Ti-s inverted fluorescence microscope, Nanofiber films were obtained using the ET-2523X-Elite electrospinning machine, mass spectra were obtained using an Agilent 1290-Bruker microTOF Q II high-resolution mass spectrometer.

2.3 Synthesis and characterization of the PPBD

The synthetic route of compound **PPBD** is shown in Fig. 1. Compound (**1**) was synthesized following the method of Tao *et al.*,[36] with specific steps referred to in the ESI† (ESI 1.1). Compound (**3**) was synthesized following the method of Nie *et al.*,[37] with specific steps referred to in the ESI 1.2 (ESI†).

2.3.1. Synthesis of 9-(5-(4,4,5,5-tetramethyl-1,3,2-dioxaborolan-2-yl)pyridin-2-yl)-9*H*-carbazole (2). The compound (**1**) (100 mg, 0.3 mmol), bis(pinacolato)diboron (229 mg, 0.9 mmol), potassium acetate (178 mg, 1.2 mmol), and $pd(dppf)Cl_2$ (22 mg, 0.03 mmol) were dissolved in dry toluene (5 mL). After three cycles of degassing, the reaction mixture was stirred at 115 °C under a nitrogen atmosphere for 6 hours. By column chromatography (*n*-hexane : ethyl acetate, v : v = 50 : 1), the desired compound (**2**) was obtained as light solid (108 mg, 98% yield). ^{1}H NMR (400 MHz, $CDCl_3$): δ 9.06 (s, 1H), 8.32-8.25 (m, 1H), 8.11 (d, J = 7.7, 1.0 Hz, 2H), 7.89 (d, J = 8.4 Hz, 2H), 7.64 (d, J = 8.0, 0.9 Hz, 1H), 7.48–7.40 (m, 2H), 7.36–7.28 (m, 2H), 1.40 (s, 12H); ^{13}C NMR (100 MHz, $CDCl_3$): δ 155.81, 144.72, 139.47, 126.33, 121.19, 120.22, 117.91, 111.54, 83.54, 25.09. HRMS (ESI): calcd for $C_{35}H_{21}N_3O_2$, $[M+H]^+$: 370.1925; found, 370.1980.

2.3.2. Synthesis of 6-(6-(9*H*-carbazol-9-yl)pyridin-3-yl)-2-phenyl-1*H*-benzo[*de*]isoquinoline-1,3(2*H*)-dione (PPBD). The compound (**2**) (100 mg, 0.28 mmol), compound (**3**) (220 mg, 0.56 mmol), copper(I) chloride (28 mg, 0.28 mmol), cesium carbonate (182 mg, 0.56 mmol), dppf (16 mg, 0.028 mmol), and $Pd(OAc)_2$ (4 mg, 0.05 mmol) were dissolved in dry DMF (5 mL). After three cycles of degassing, the reaction mixture was stirred at 100 °C under a

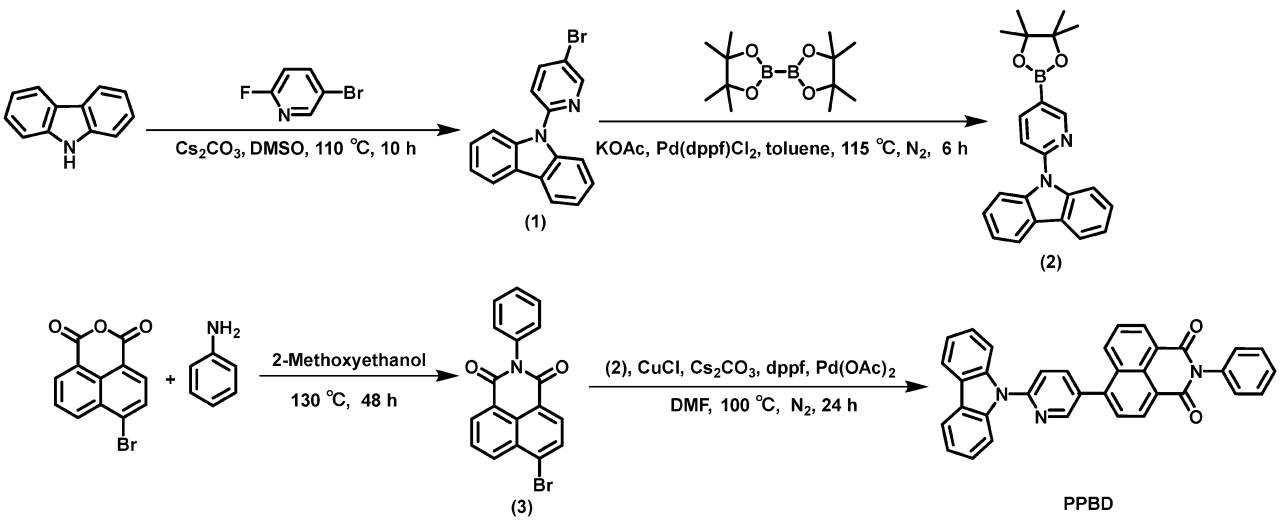

Fig. 1 Synthetic route of compound **PPBD**.

nitrogen atmosphere for 24 hours. By column chromatography (petroleum ether: ethyl acetate, v : v = 30 : 1), the desired compound **PPBD** was obtained as greenish-yellow solid (40 mg, 32% yield). ^{1}H NMR (400 MHz, $CDCl_3$): δ 8.91 (d, J = 2.5 Hz, 1H), 8.78 (d, J = 7.5 Hz, 1H), 8.76 (d, J = 7.4 Hz, 1H), 8.42 (d, J = 8.5 Hz, 1H), 8.17 (d, J = 7.8 Hz, 2H), 8.15–8.11 (m, 1H), 8.04 (d, J = 8.3 Hz, 2H), 7.89 (t, J = 2.6 Hz, 2H), 7.86 (d, 1H), 7.59 (t, J = 8.4, 6.8 Hz, 2H), 7.51 (t, J = 7.5, 1.3 Hz, 2H), 7.40 (s, 1H), 7.39–7.35 (m, 4H). ^{13}C NMR (100 MHz, $CDCl_3$): δ 164.46, 164.40, 151.88, 149.82, 140.17, 136.59, 135.67, 135.16, 132.12, 131.86, 131.57, 130.40, 130.32, 129.90, 129.38, 128.52, 128.45, 127.29, 124.59, 123.39, 121.76, 121.09, 118.07, 111.95. HRMS (ESI): calcd for $C_{35}H_{21}N_3O_2$, $[M+H]^+$: 516.1707; found, 516.1715.

2.4. Preparation of PPBD/PEO electrospun fiber films

In this study, the resulting probe **PPBD** was electrospun with PEO to make nanofiber films. Dissolve **PPBD** (2.5 mg) completely in DMF (5 mL), then add 250 mg of PEO to the solution. Stir the mixture until it becomes transparent, and then let it stand at room temperature for 2 hours. Transfer the prepared solution into a standard 5 mL glass syringe, attaching a stainless steel needle (inner diameter = 0.63 mm) to the front end as the nozzle. Connect the positive terminal of the high-voltage power supply to the nozzle and the negative terminal to a metal collection device, the electrospinning operation was performed. In this study, the electrospinning conditions were optimized. The main factors affecting the electrospinning include the injection pump feed rate, positive and negative voltage, relative humidity, temperature, and the distance of the nozzle from the receiver. This experiment conducted univariate experiments on the above influencing factors, and the specific variables are shown in Table S1 (ESI†). Set the electrospinning apparatus parameters as follows: room temperature (25 °C) and a relative humidity of 10%, set positive voltage to 12 kV, negative high voltage to −2.5 kV, nozzle-to-collector distance of 20 cm, syringe pump feed rate of 0.3 mm min^{-1}, and electrospin continuously for 2 hours. Collect the electrospun polymer fibers on aluminum foil to obtain **PPBD**/PEO electrospun fibers. The preparation process of the electrospun nanofiber sensor is shown in the Fig. 2.

2.5. Detection method for fluorescence sensing performance of PPBD/PEO fiber thin films

2.5.1. Fluorescence testing at saturation vapor pressure. Place a small amount of the analyte (15 mg of solid or 15 μL of liquid) into a crucible (5 mm × 2.5 mm) and position the crucible at the bottom of a quartz cuvette (1 cm × 1 cm × 3.5 cm). Seal the cuvette and let it stand at room temperature for 12 hours to reach the saturation vapor pressure. Under room temperature conditions, collect the fluorescence data of the film before and after exposure to the analyte vapor at an excitation wavelength of 308 nm.

2.5.2. Calculation of fluorescence quenching efficiency. To compare the performance of different fluorescence sensors, the fluorescence quenching rate (FQR) was calculated using Formula (1).

$$\mathrm{FQR} = (I_0 - I)/I_0 \quad (1)$$

I_0: the initial fluorescence intensity of the film; I: the fluorescence intensity after exposure to the explosive vapor.

3. Results and discussion

3.1 Photophysical properties of the PPBD

First, the photophysical properties of **PPBD** were investigated, as shown in Fig. 3. The absorption peaks of **PPBD** in chloroform are located at 345 nm and 387 nm, with a strong emission peak at 515 nm. The emission spectrum of the **PPBD** fiber film shows a distinct emission peak at 612 nm. Compared to the chloroform solution of **PPBD**, the emission peak of the **PPBD** fiber film is red-shifted by 97 nm, which may be due to more pronounced π–π stacking of the molecule in the fiber state than in the solution state. From Fig. 3, it can be observed that the excitation spectrum of the **PPBD** fiber film has a narrower peak width compared to that of the solution, indicating that the **PPBD** fiber film has a higher selectivity for the wavelength of the excitation light. This helps to reduce non-specific fluorescent interference, enhancing the specificity and accuracy of the detection. This is associated with a high fluorescence quantum yield, which endows the fluorescent probe with superior photosensitivity

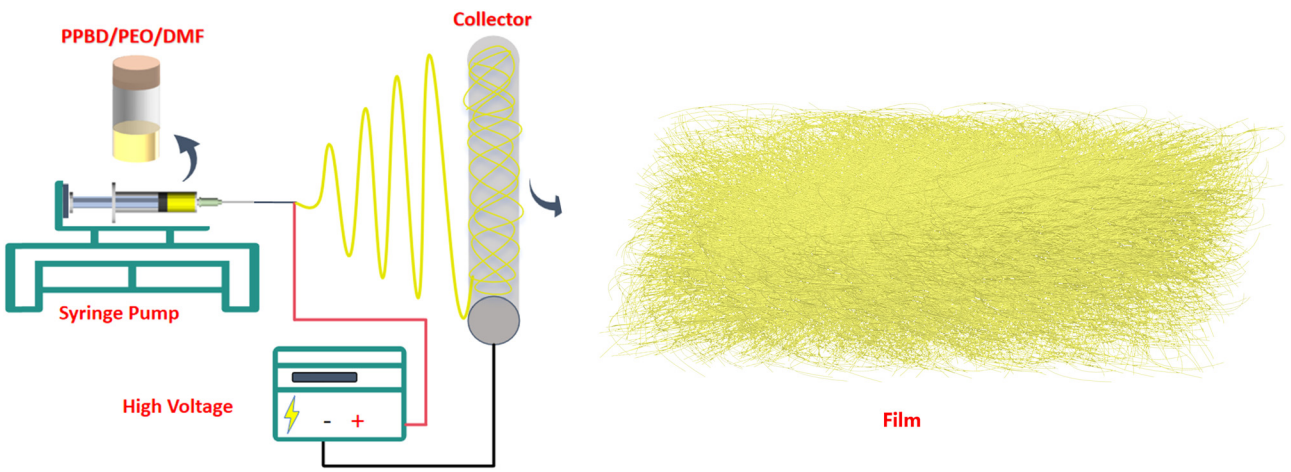

Fig. 2 Schematic diagram of the electrospinning thin film preparation.

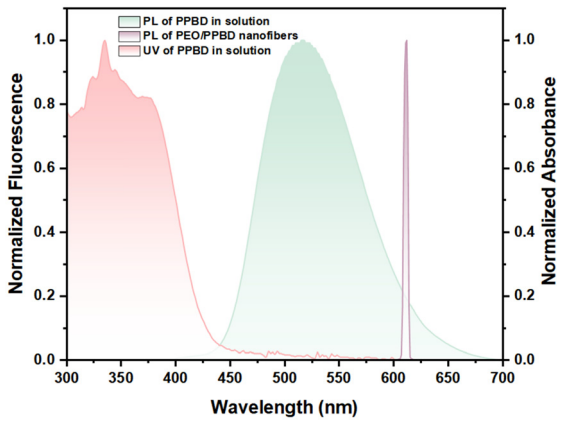

Fig. 3 Absorption and fluorescence spectra of **PPBD** in solution (λ_{ex} = 308 nm) and fluorescence spectra of **PPBD**/PEO electrospun fibers (λ_{ex} = 308 nm).

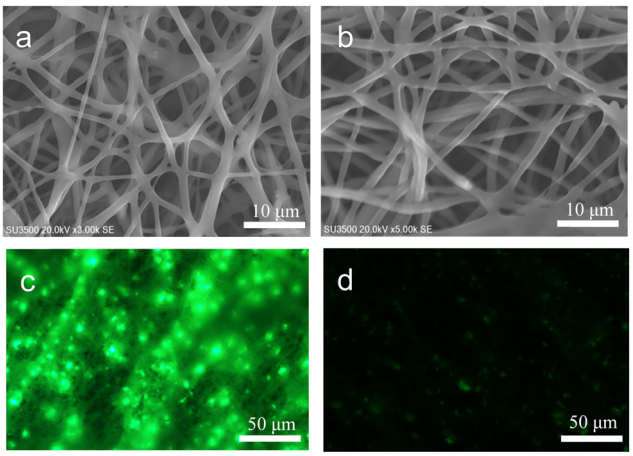

Fig. 4 (a) Scanning electron microscopy (SEM) diagram, pure PEO nanofiber morphology. (b) SEM diagram, PEO nanofiber morphology mixed with **PPBD**. (c) Fluorescence microscopy (FL) diagram of **PPBD** nanofiber film exposed to HMX vapor. (d) FL diagram of **PPBD** nanofiber film exposed to HMX vapor after 2 hours.

and sensitivity in the field of bioanalysis. Probes with a narrow excitation band are less susceptible to the influence of solvent polarity and refractive index in the absence of interfering groups, a property of significant importance for the design of fluorescent probes that can function in various solvents. Their narrow excitation bands are typically accompanied by narrow fluorescence spectrum peak widths, which aid in distinguishing different fluorescent signals in multiplex fluorescence analysis, reducing signal overlap and interference. At the same time, narrow excitation bands facilitate more effective separation and detection of target molecules in complex biological samples by reducing non-specific binding and background noise.

In summary, the narrow excitation band is an important characteristic of the **PPBD** nanofibers developed in this experiment. It helps to improve the selectivity, sensitivity, and signal-to-noise ratio of fluorescence detection, which is crucial for the application of fluorescent probes in biomedical research and clinical diagnostics.

3.2. Physical morphology characterization of PPBD/PEO electrospun fibers

The efficient quenching reaction of **PPBD** probes with explosives encouraged us to investigate their practical applicability in the field detection of these analytes. Therefore, **PPBD** nanofibers were prepared by electrospinning, and the resulting **PPBD** nanofibers exhibited a well-defined fiber morphology with excellent structural stability. As shown in Fig. 4a and b, the morphology of the nanofibers doped with **PPBD** remained unchanged, and both showed a smooth surface and uniform thickness, similar to that of pure PEO nanofibers.

To confirm the distribution of the organic small molecule **PPBD** in the **PPBD**/PEO polymer luminescent fibers, fluorescence microscopy was performed on the nanofibers after **PPBD** incorporation. As shown in Fig. 4c, the **PPBD**/PEO electrospun nanofibers exhibit uniformand bright fluorescence before quenching, indicating successful and uniform distribution of **PPBD** within the PEO matrix. From Fig. 4d, it is clear that after placing the sensor in saturated HMX vapor (10 ppb) for 2 hours, the fluorescence of the **PPBD**/PEO electrospun nanofibers is completely quenched.

3.3. Characterization of the optical properties of PPBD/PEO electrospun fibers

3.3.1. Fluorescence quenching efficiency of electrospun films. Subsequently, the sensing performance of the **PPBD**/PEO electrospun fibers was investigated. PETN, an explosive, was selected as a fluorescence quencher, and a series of fluorescence quenching experiments were conducted in an air environment. Fig. 5a presents the fluorescence spectra of the **PPBD**/PEO (**PPBD** content of 1.0 wt%) electrospun fibers in PETN vapor. Under ambient air conditions, we exposed the **PPBD**/PEO polymer fiber membrane to saturated PETN vapor for 2 hours and collected fluorescence spectra at different quenching times. As shown in Fig. 5a, the fluorescence intensity decreases with increasing quenching time, the fluorescence intensity after quenching stabilized after 90 minutes.

The FQR was calculated using Formula (1), it was determined that after 5 minutes, the fluorescence intensity quenching efficiency of the **PPBD**/PEO polymer fibers reached 50.7% (Fig. S1, ESI†), and after 2 hours, the fluorescence quenching efficiency reached 64% (Fig. S1, ESI†). Fig. S1 (ESI†) shows the fluorescence quenching efficiency *versus* time plot of electrospun films doped with different **PPBD** content. Although the quality fraction of **PPBD** is as low as 1 wt% in the **PPBD**/PEO fiber film, the fluorescence quenching efficiency is as high as 64%. To achieve a sensor with higher quenching efficiency, the content of **PPBD** in the **PPBD**/PEO polymer fibers was increased. Excitingly, when the fiber film with a **PPBD** content of 5.0 wt% was exposed to PETN vapor for 2 hours (Fig. 5c), its fluorescence quenching efficiency reached 72% (Fig. S1, ESI†). By merely doubling the content of **PPBD** in the nanofibers from 1.0 wt% to 5.0 wt%, the quenching efficiency was increased by 1.125 times. This indicates that the quenching efficiency of the explosives can be increased by

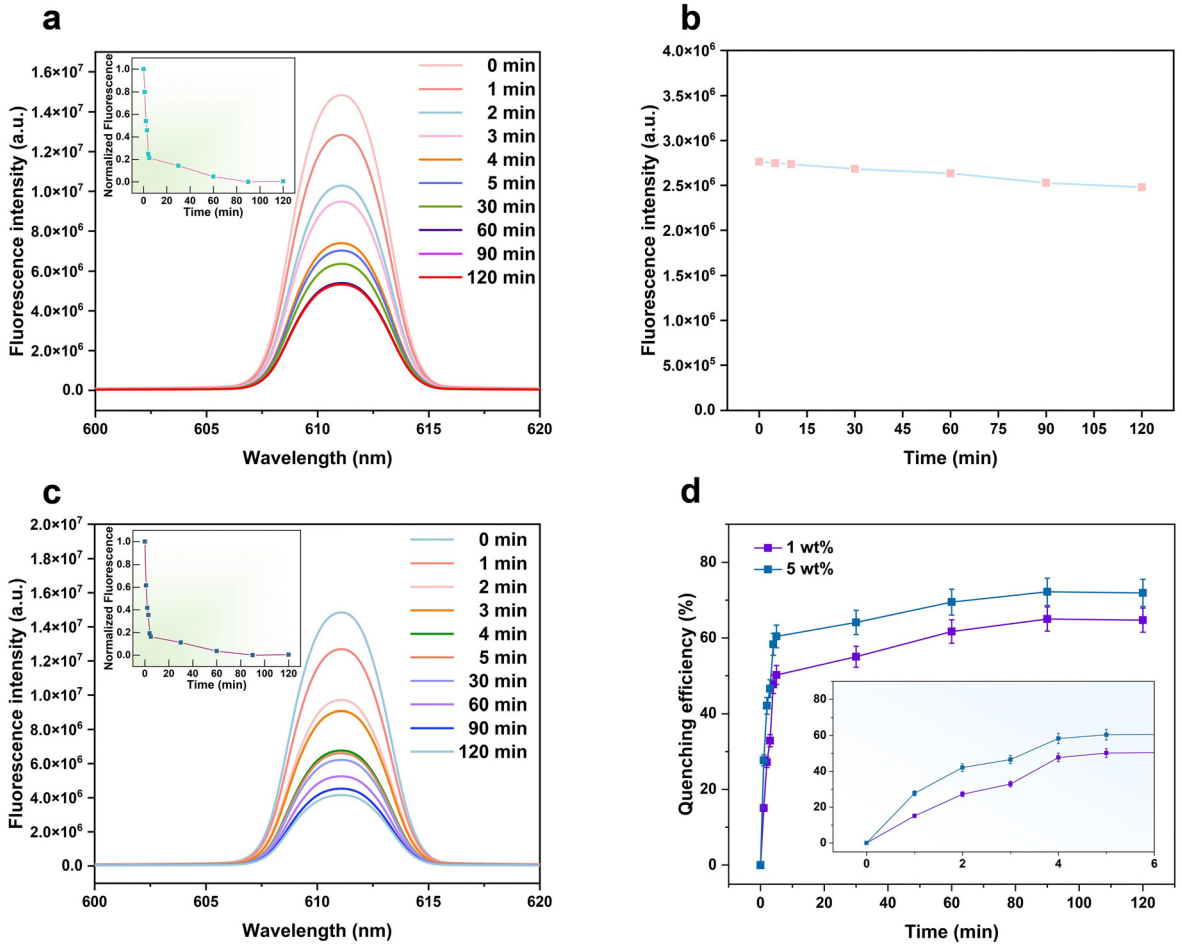

Fig. 5 Fluorescence spectrum (a) fluorescence spectrum of **PPBD**/PEO fiber film (1 wt%) in PETN vapor. (b) Fluorescence intensity in air curve (λ_{ex} = 308 nm). (c) Fluorescence spectrum of the PEO/**PPBD** fiber film (5.0 wt%) in PETN vapor (λ_{ex} = 308 nm). (d) Fluorescence quenching efficiency of PPB/PEO polymer fiber film on analytes and the quenching efficiency curves *versus* exposure time with standard deviation error bars of three batches prepared at different times.

increasing the content of the probe in the film, making the quenching effect more significant. Moreover, we prepared three batches of probes to detect PETN, and the quenching efficiency is shown in Fig. 5d. The specific fluorescence spectra data can be found in ESI,† Fig. S2. As can be seen from Fig. 5d, the detection of PETN by probes from different batches is relatively stable.

There optical fluorescent nanofiber materials reported that are able to detect RDX and PETN and even rare for HMX. According to the literature,[38] novel sensing materials have been developed *via* nanomaterial synthesis for specific detection of the aforementioned explosive analytes, but it did not provide specific quenching efficiencies of these explosive analytes on the manufactured nanofiber materials. Surprisingly, our low-cost sensing material can "sniff" all them out, suggesting the ultrasensitivty of the developed sensing material for broad spectrum of explosives. This suggests that **PPBD** has the potential to be a high-performance fluorescent sensor. Meanwhile, this provides a feasible scheme for the detection of PETN, HMX and so on. In an air environment without PETN, the fluorescence spectra of the **PPBD**/PEO fiber film were collected at different time intervals, and the fluorescence intensity change over time was plotted (Fig. 5b). This served as a control experiment to confirm that the fluorescence quenching resulted from the interaction between the **PPBD**/PEO fiber film and PETN. From Fig. 5b, under excitation with light at the same wavelength (308 nm), the fluorescence intensity of the **PPBD**/PEO polymer fiber film remains virtually unchanged, indicating that the fluorescence quenching of the **PPBD**/PEO polymer fiber film is caused by its interaction with PETN vapor.

3.3.2. Sensor selectivity and sensitivity testing. To investigate the selectivity of the **PPBD**/PEO fiber film in detecting analyte vapors, the same batch of **PPBD**/PEO fiber films prepared was exposed to the saturated vapors of 11 analytes, including HMX, TNT, RDX, PETN, 2-nitro-*m*-xylene, water, benzene, phenol, fragrance, urea, and sodium nitrate ($NaNO_2$), for 2 hours at room temperature (for specific fluorescence spectra, please refer to Fig. S3 and S4, ESI†). Fluorescence spectra of the **PPBD**/PEO polymer fiber membrane were collected and the fluorescence quenching efficiency was calculated (according to Formula (1)), with the results plotted in the fluorescence quenching efficiency graph as shown in Fig. 6. The graph reveals that the **PPBD**/PEO fiber film exhibited significant fluorescence quenching ability towards the five nitro compounds (HMX, PETN, TNT, RDX, 2-nitro-*m*-xylene),

with fluorescence quenching efficiencies all above 40%, and HMX reaching as high as 92%.

In the present study, the fluorescent nanomaterials synthesized by our research team have demonstrated superior fluorescence quenching efficiency in the detection of HMX analytes, surpassing slightly the 91% quenching efficiency achieved by the compound 3-ODC in previous studies.[39] This accomplishment signifies a remarkable advancement in the design and synthesis of fluorescent nanomaterials, particularly in enhancing the sensitivity of explosive detection. Furthermore, we have transformed the synthesized compounds into fibrous films through electrospinning technology. Compared to traditional solution-based fluorescent probes, these film fibers offer significant advantages, including portability, stability, and flexibility. Portability implies that these films can be readily applied across various detection scenarios. Stability ensures consistent performance under diverse environmental conditions, while flexibility allows the films to conform to different surfaces and shapes, thereby expanding their scope of application.

The combination of these characteristics of the film fibers, along with their high-sensitivity fluorescence quenching efficiency, indicates a broad application prospect for films manufactured by the integration of fluorescent probes and nanospinning technology in the field of explosive detection. This novel material is not only capable of increasing detection efficiency but also has the potential to play a significant role in multiple domains, including public safety, national defense, and environmental monitoring. With further research and development, we anticipate that these fluorescent nanomaterials will provide robust technical support for the rapid and accurate detection of explosives. The fluorescence quenching efficiency follows the order: HMX > TNT> RDX >PETN >2-nitro-*m*-xylene. In contrast, negligible fluorescence quenching was observed for the interfering analytes, including water, benzene, phenol, urea, $NaNO_2$, and fragrance.

These results clearly demonstrate that the **PPBD**/PEO fiber film sensor exhibits a high degree of selectivity for nitroaromatic compounds. The sensitivity of the sensor, as one of the key parameters for assessing its performance, can be quantified using the fluorescence static quenching coefficient (K_{sv}). It can be calculated according to the Stern–Volmer[40] Formula (2) equation.

$$I_0/I = 1 + K_{sv}[Q] \quad (2)$$

I_0 and I are the fluorescence intensities in the absence and presence of the analyte/explosive, respectively; K_{sv} is the quenching constant, and [Q] is the concentration of the quencher. K_{sv} is the Stern–Volmer constant, a physical quantity used to measure the sensitivity of a fluorescent material to analyte detection. Under the same conditions, the larger the K_{sv} value, the higher the quenching sensitivity of the corresponding fluorescent material. When the concentration of HMX is 6.6×10^{-3} mol L^{-1}, the fluorescence quenching efficiency of the **PPBD** sensor is 92%, thus K_{sv} is calculated to be 1.8×10^3 mol L^{-1}, indicating that the **PPBD** sensor exhibits good sensitivity. The limit of detection (LOD) of **PPBD** in HMX can be obtained from the equation of Formula (3).

$$LOD = 3S/K_{sv} \quad (3)$$

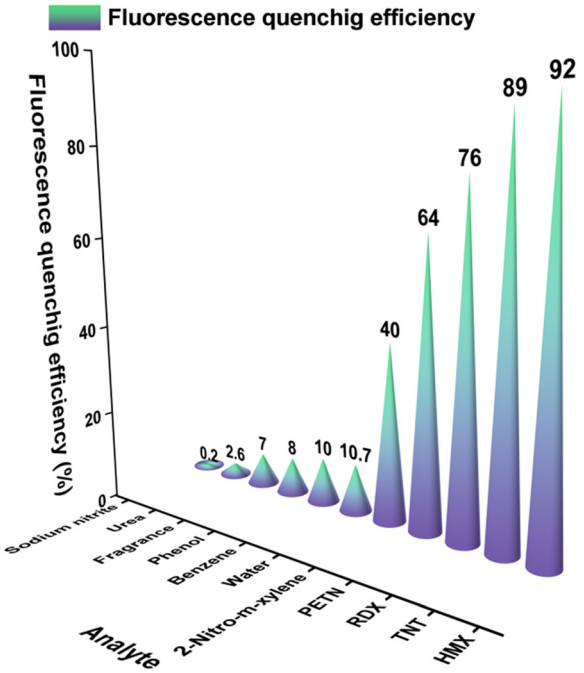

Fig. 6 Fluorescence quenching efficiency of PPB/PEO polymer fiber film on analytes.

where S is the standard deviation (SD) of the fluorescence intensity for the blank samples which has been measured 5 times, thus LOD is calculated to be 7.85×10^{-2} mol L^{-1}. The sensor **PPBD** showed a number of attractive characteristics such as good selectivity, high sensitivity and wide applicability. Please refer to Table 1 for the K_{sv} values and LOD corresponding to each analyte.

3.4. Explanation of the sensor mechanism

To investigate the interaction between **PPBD** and the analyte, the ^{1}H NMR spectra of **PPBD** before (Fig. 7a) and after (Fig. 7b) the addition of HMX were compared. As shown in Fig. 7b, Upon adding HMX to **PPBD** in $CDCl_3$, the chemical shifts of the majority of hydrogen atoms exhibited alterations, with some experiencing downfield shifts and others upfield shifts. These results suggest that the HMX molecule protonates **PPBD**, resulting in strong electrostatic interactions between protonated **PPBD** and the HMX anion.

In this study, we explored the mechanism of fluorescence quenching when **PPBD** molecules complex with explosive molecules such as HMX, TNT, RDX, PETN, and 2-nitro-*m*-xylene through molecular dynamics simulation and energy level matching analysis. This research utilized molecular dynamics simulation to model the binding process of **PPBD** molecules with explosive molecules, as their spatial arrangements are infinitely diverse and cannot be calculated through traditional exhaustive methods. Through simulation, we recorded the thermal motion and binding trajectories of the molecules, optimized the conformations, and ultimately obtained the optimal conformation representing the stability of the complex. We calculated the HOMO and LUMO energy levels of **PPBD** molecules and explosive molecules, and the results can be seen in Fig. 8, which shows that the LUMO energy

Table 1 The K_{sv} values and LOD corresponding to each analyte

Exploder	Explosives structure	K_{sv} (M^{-1})	(LOD) (M)
HMX	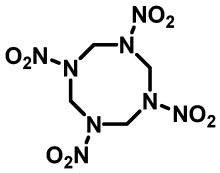	1.8×10^3	7.85×10^{-2}
PETN	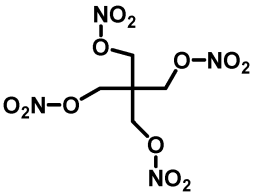	327	0.154
RDX	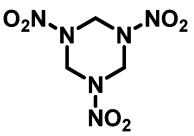	3.95×10^3	1.56×10^{-2}
TNT	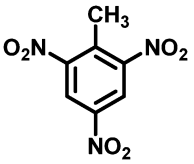	1.08×10^3	6.4×10^{-2}
2,6-Dimethylnitrobenzene	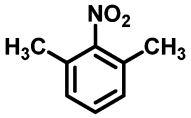	95	0.22

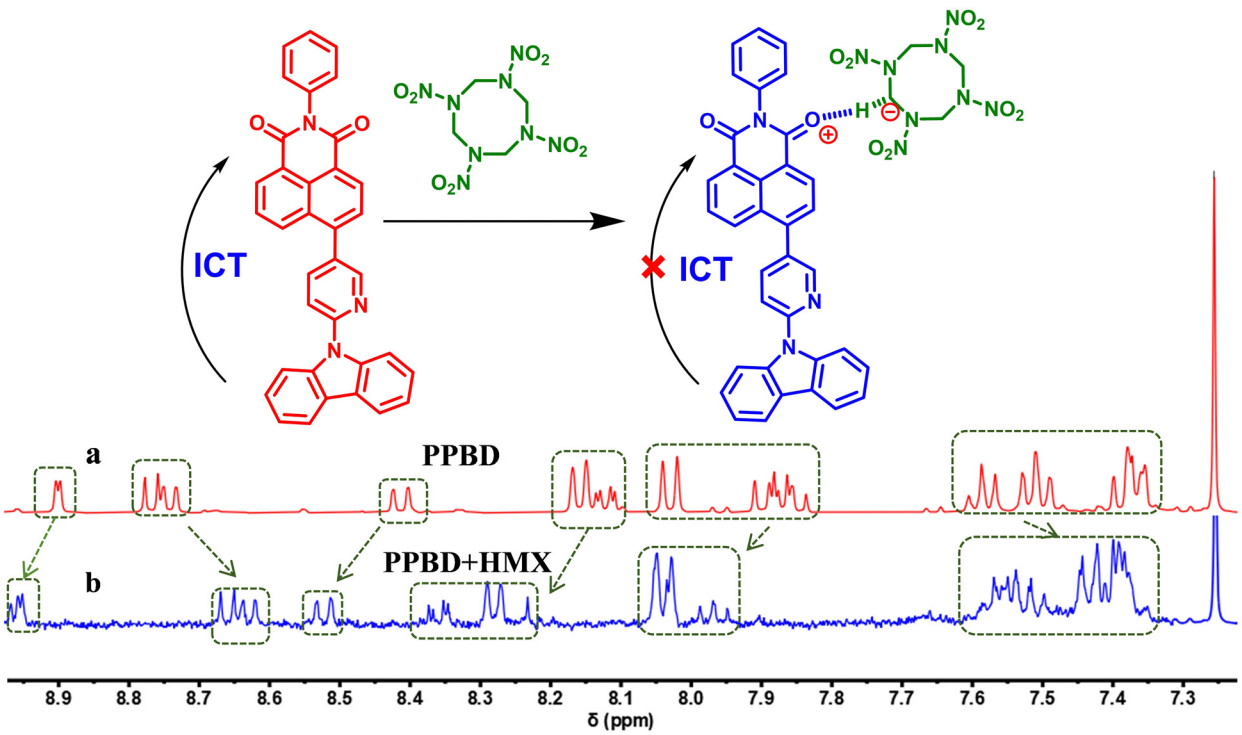

Fig. 7 ^{1}H NMR of **PPBD** in $CDCl_3$ before (a) and after (b) the addition of HMX.

level of **PPBD** is −2.84 eV, while the LUMO energy level of HMX is −3.54 eV, proving that the LUMO energy level of **PPBD** is indeed higher than that of HMX, thus supporting the occurrence of electron transfer. This result provides a theoretical basis for the mechanism of fluorescence quenching of **PPBD** molecules in the complex. Additionally, TNT, RDX, PETN, and 2-nitro-*m*-xylene also show similar energy level matching relationships, further validating the impact of energy level matching on fluorescence quenching. The optimal conformation revealed that the binding of explosive molecules with **PPBD** molecules is mainly achieved through π–π interactions, where the parallel arrangement between the two molecules helps to form strong π–π interactions, enhancing the stability of the complex.

This study analyzed the weak interactions between **PPBD** and explosive molecules, such as π–π stacking and electrostatic interactions, and found significant mutual attraction between **PPBD** and HMX molecules. To quantitatively analyze these changes, we used the root-mean-square deviation (RMSD) method to compare the conformational differences of **PPBD** in its free state and in the complex. The smaller the RMSD value, the more similar the conformations are. By calculating the RMSD between **PPBD** molecules in the complex and their free state, we were able to assess the conformational changes of **PPBD** molecules in the complex. The analysis showed that there are certain differences in the conformational changes of **PPBD** after binding with HMX, TNT, RDX, PETN, and 2-nitro-*m*-xylene. For instance, the RMSD values for TNT, RDX, and PETN are 2.62, 2.28, and 2.26, respectively, indicating significant conformational changes; whereas in the complexes with HMX and 2-nitro-*m*-xylene, the conformational changes of **PPBD** molecules are relatively smaller, with RMSD values of 1.96 and 1.94, respectively, which may suggest a stronger interaction between HMX and **PPBD**, thereby reducing conformational changes. These findings collectively support the establishment of electron transfer theory and provide important theoretical guidance for the future design of fluorescence molecules based on energy level matching and their quenching mechanisms. Future research can further explore the impact of different explosive molecules on the fluorescence properties of **PPBD** and verify these computational results through experiments.

4. Conclusions

This study provides a comprehensive exposition of the synthesis process of the fluorescent probe **PPBD** and the innovative method of preparing fluorescent nanofiber sensors through electrospinning technology. The experimental data clearly demonstrate that the prepared nanofibers not only fully retain the inherent luminescent properties of the **PPBD** molecules but also significantly enhance sensitivity and selectivity in the detection process. When these nanofiber sensors are exposed to an environment saturated with explosive vapors, they respond rapidly and exhibit a pronounced fluorescence quenching phenomenon. Further experiments, by adjusting the content of **PPBD** in the nanofibers from 1.0 wt% to 5.0 wt%, observed a steady increase in fluorescence quenching efficiency. In selective tests against a range of explosives

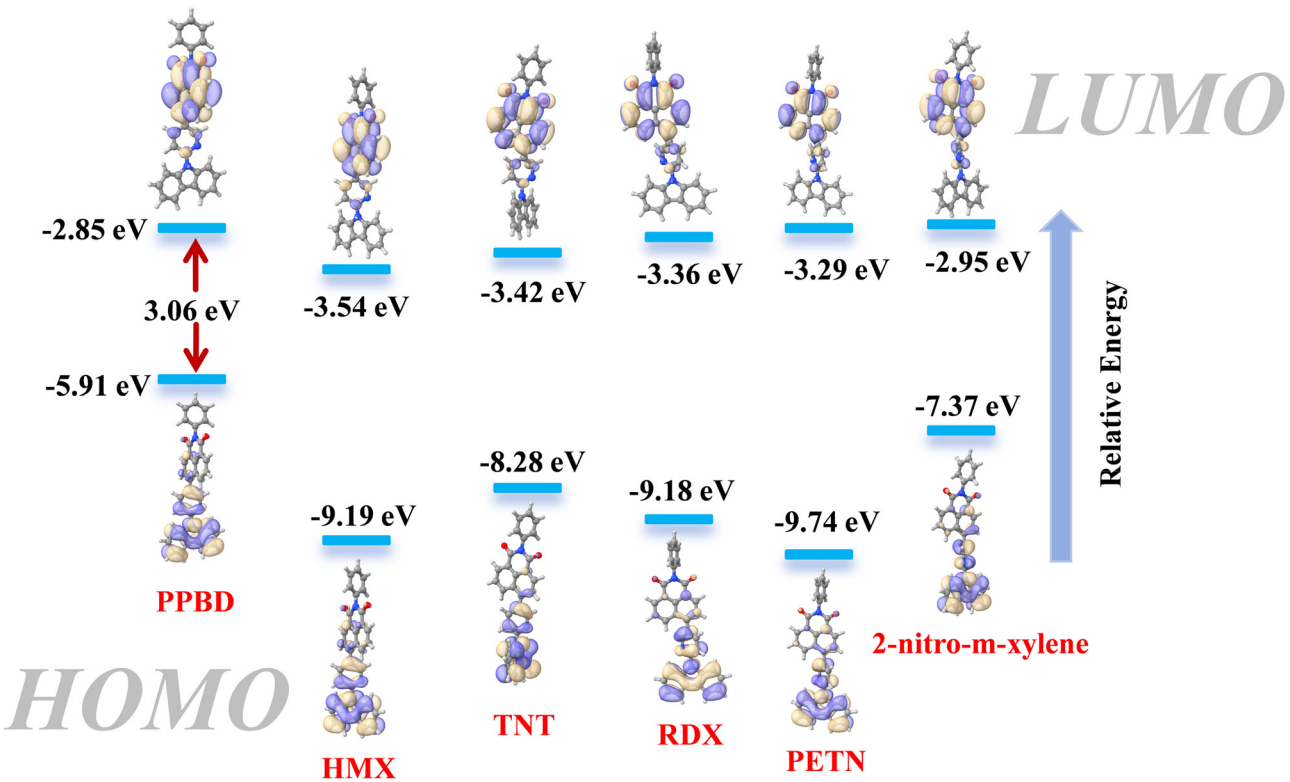

Fig. 8 Energy level diagrams of the LUMO and HOMO orbitals for **PPBD**, HMX, TNT, RDX, PETN, and 2-nitro-*m*-xylene.

including HMX, TNT, RDX, PETN, and 2-nitro-*m*-xylene, the sensors were able to significantly quench the fluorescence signals of these compounds. Specifically, the quenching efficiencies for HMX, TNT, RDX, PETN, and 2-nitro-*m*-xylene vapors reached 92%, 89%, 76%, 64%, and 40%, respectively, with the most outstanding selectivity for HMX vapor.

Additionally, the form of fiber films facilitates on-site detection of explosives. Compared to solutions, the narrower peak width of the excitation spectrum indicates that the **PPBD** fiber film has a higher selectivity for the wavelength of the excitation light. This enhanced selectivity was attributed to the increased contact area between the nanofibers and the analyte in the membrane, which more effectively blocked the ICT emission, leading to fluorescence quenching. This characteristic effectively reduces non-specific fluorescent interference, thereby enhancing the specificity and accuracy of detection. In the field of bioanalysis, this fluorescent probe with high photosensitivity and sensitivity shows great potential for application. It is worth noting that under conditions lacking interfering groups, the **PPBD** probe's characteristic of a narrow excitation band makes it less sensitive to changes in solvent polarity and refractive index. This feature is of significant guidance for the development of fluorescent probes that can stably function in a variety of solvent environments, providing a new direction for future research and applications in related fields.

Author contributions

The manuscript was written through contributions of all authors. All authors have given approval to the final version of the manuscript.

Data availability

The data supporting this article have been included as part of the ESI.†

Conflicts of interest

There are no conflicts to declare.

Acknowledgements

This study was performed under financial support by the Program of Science and Technology Development Plan of Jilin Province (YDZJ202201ZYTS618, YDZJ202301ZYTS312). General Project of Jilin Provincial Department of Education Science and Technology Research Project (JJKH20240301KJ), Outstanding Youth Training Program of Jilin City (20230103015).

References

1 H. De Cauwer, D. G. Barten, D. Tin, L. J. Mortelmans, G. R. Ciottone and F. Somville, *Prehosp. Disaster Med.*, 2023, **38**, 33–40.
2 S. Mary Celin, B. Sharma, P. Bhanot, A. Kalsi, S. Sahai and R. K. Tanwar, *Mass Spectrom. Rev.*, 2023, **42**, 1727–1771.
3 C. Zhang, X. Pan, H. Deng, S. Cheng, A. Xie and W. Dong, *J. Lumin.*, 2021, **238**, 118318.
4 J. Wang, W. Liu, G. Luo, Z. Li, C. Zhao, H. Zhang, M. Zhu, Q. Xu, X. Wang, C. Zhao, Y. Qu, Z. Yang, T. Yao, Y. Li, Y. Lin, Y. Wu and Y. Li, *Energy Environ. Sci.*, 2018, **11**, 3375–3379.
5 L. Ding and Y. Fang, *Chem. Soc. Rev.*, 2010, **39**, 4258–4273.
6 X. Jiang, H. Li, Q. Zhou, Q. Wei, M. Wei, L. Jiang, Z. Wang, Z. Peng, F. Wang, Z. Zang, K. Xu, Y. Hou, S. Teale, W. Zhou, R. Si, X. Gao, E. H. Sargent and Z. Ning, *J. Am. Chem. Soc.*, 2021, **143**, 10970–10976.
7 J. Hu, Y. Q. Liang, S. L. Wu, Z. Y. Li, C. S. Shi, S. Y. Luo, H. J. Sun, S. L. Zhu and Z. D. Cui, *Mater. Today Nano*, 2022, **17**, 100150.
8 C. Byram, S. S. B. Moram and V. R. Soma, *Analyst*, 2019, **144**, 2327–2336.
9 W. Xu, Y. Chen, H. Zhan and J. N. Wang, *Nano Lett.*, 2016, **16**, 946–952.
10 D. S. Moore and R. J. Scharff, *Anal. Bioanal. Chem.*, 2009, **393**, 1571–1578.
11 M. Liszewska, B. Bartosewicz, B. Budner, B. Nasiłowska, M. Szala, J. L. Weyher, I. Dzięcielewski, Z. Mierczyk and B. J. Jankiewicz, *Vib. Spectrosc.*, 2019, **100**, 79–85.
12 J. Wu and Y. Hong, *Bioact. Mater.*, 2016, **1**, 56–64.
13 J. Qu, Y. Ge, B. Zu, Y. Li and X. Dou, *Small*, 2016, **12**, 1369–1377.
14 W. Li, Z. Li, C. Si, M. Y. Wong, K. Jinnai, A. K. Gupta, R. Kabe, C. Adachi, W. Huang, E. Zysman-Colman and I. D. W. Samuel, *Adv. Mater.*, 2020, **32**, e2003911.
15 J. Tang, J. Wu and Y. He, *Forensic Chem.*, 2024, **38**, 100568.
16 Z. Mo, D. Tai, H. Zhang and A. Shahab, *Chem. Eng. J.*, 2022, **443**, 136320.
17 C. Zhang, S. Cheng, Q. Zhuang, A. Xie and W. Dong, *New J. Chem.*, 2022, **46**, 1896–1904.
18 O. S. Taniya, A. F. Khasanov, L. K. Sadieva, S. Santra, I. L. Nikonov, W. K. A. Al-Ithawi, I. S. Kovalev, D. S. Kopchuk, G. V. Zyryanov and B. C. Ranu, *Materials*, 2023, **16**, 6333.
19 Y. Ke, X. Zhu, W. Ren, B. Zu and X. Dou, *Sci. Sin.: Chim.*, 2020, **50**, 3–17.
20 A. Pantazis, K. Westerberg, T. Althoff, J. Abramson and R. Olcese, *Nat. Commun.*, 2018, **9**, 4738.
21 K.-Y. Huang, W.-H. Weng, X. Huang, H.-X. Huang, H. A. A. Noreldeen, H.-H. Deng and W. Chen, *Nanomaterials*, 2022, **12**, 1861.
22 M. Duan, X. Xiao, Y. Huang, G. Li, S. Shan, X. Lv, H. Zhou, S. Peng, C. Liu and D. Liu, *Food Chem.*, 2021, **334**, 127568.
23 X. Cheng, Y. Yan, X. Chen, J. Duan, D. Zhang, T. Yang, X. Gou, M. Zhao, S. Ding and W. Cheng, *Sens. Actuators*, 2021, **331**, 129458.
24 C. Chen, S. A. Boulanger, A. I. Sokolov, M. S. Baranov and C. Fang, *Chemosensors*, 2021, **9**, 234.
25 S. Halder, R. Aggrawal, V. K. Aswal, D. Ray and S. K. Saha, *J. Mol. Liq.*, 2021, **322**, 114532.
26 J.-L. Wu, C. Zhang, W. Qin, D.-P. Quan, M.-L. Ge and G.-D. Liang, *Chin. J. Polym. Sci.*, 2019, **37**, 394–400.
27 F. Cui, Z. Xie, R. Yang, Y. Zhang, Y. Liu, H. Zheng and X. Han, *Spectrochim. Acta, Part A*, 2024, **314**, 124222.

28 D. Wang, F. Gao, X. Wang, X. Ning, K. Wang, X. Wang, Y. Wei and T. Fujita, *Toxics*, 2022, **10**, 367.
29 J. Wang, Y. Feng, X. Zhao, Y. Tian and Y. Duan, *Biosens. Bioelectron.*, 2023, **238**, 115562.
30 W. Wu, N. Shi, J. Zhang, X. Wu, T. Wang, L. Yang, R. Yang, C. Ou, W. Xue and X. Feng, *J. Mater. Chem. A*, 2018, **6**, 18543–18550.
31 W. Xue, Y. Zhang, J. Duan, D. Liu, Y. Ma, N. Shi, S. Chen, L. Xie, Y. Qian and W. Huang, *J. Mater. Chem. C*, 2015, **3**, 8193–8199.
32 Y. Yang, H. Wang, K. Su, Y. Long, Z. Peng, N. Li and F. Liu, *J. Mater. Chem.*, 2011, **21**, 11895–11900.
33 A. Santos, G. O. Deokaran, C. V. Costa, L. Gama, E. G. Mazzini Júnior, A. M. L. de Assis, J. D. de Freitas, W. R. de Araujo, R. P. Dias, J. C. S. da Silva, L. M. M. Costa and A. S. Ribeiro, *Forensic Sci. Int.*, 2021, **329**, 111056.
34 Z. Meng, X. Li, Q. Ye, H. Wang, Y. Liang, Y. Yang, X. Xu, Z. Wang and S. Wang, *Ind. Crops Prod.*, 2024, **222**, 119522.
35 L. Hu, X. Zeng, X. Wei, H. Wang, Y. Wu, W. Gu, L. Shi and C. Zhu, *Appl. Catal., B*, 2020, **273**, 119014.
36 S. Tao, E. Ji, L. Shi, N. Liu, L. Xu and B. Dai, *Synthesis*, 2017, 5120–5130.
37 X. Nie, H. Su, X. Chen, W. Huang, L. Huang, B. Chen, H. Miao, J. Jiang, T. Wang and G. Zhang, *Chem. – Eur. J.*, 2020, **26**, 12743–12746.
38 Y. Wang, A. La, Y. Ding, Y. Liu and Y. Lei, *Adv. Funct. Mater.*, 2012, **22**, 3547–3555.
39 J.-Y. Zhang, C. Xia, H.-F. Wang and C. Tang, *J. Energy Chem.*, 2022, **67**, 432–450.
40 M. H. Gehlen, *J. Photochem. Photobiol.*, 2020, **42**, 100338.